

# High-throughput computation of Raman spectra from first principles

Mohammad Bagheri<sup>1</sup> and Hannu-Pekka Komsa<sup>1,\*</sup>

<sup>1</sup>Microelectronics Research Unit, Faculty of Information Technology and Electrical Engineering, University of Oulu, Oulu, FIN-90014, Finland

\*corresponding author(s): Hannu-Pekka Komsa (hannu-pekka.komsa@oulu.fi)

## ABSTRACT

Raman spectroscopy is a widely-used non-destructive material characterization method, which provides information about the vibrational modes of the material and therefore of its atomic structure and chemical composition. Interpretation of the spectra requires comparison to known references and to this end, experimental databases of spectra have been collected. Reference Raman spectra could also be simulated using atomistic first-principles methods but these are computationally demanding and thus the existing databases of computational Raman spectra are fairly small. In this work, we developed an optimized workflow to calculate the Raman spectra more efficiently compared to existing approaches. The workflow was benchmarked and validated by comparison to experiments and previous computational methods for select technologically relevant material systems. Using the workflow, we performed high-throughput calculations for a large set of materials (5099) belonging to many different material classes, and collected the results to a database. Finally, the contents of database are analyzed and the calculated spectra are shown to agree well with the experimental ones.

## Background & Summary

Raman spectroscopy is a widely used, powerful, and nondestructive tool for analysis and identification of materials as well as assessing material quality. It is based on characterization of the vibrational modes of materials and provides rich atom- or chemical bond-specific information about the crystal structure and chemical composition. When used in assessing material quality, Raman spectra contains information about grain sizes, defect densities, and strain, among others<sup>1-4</sup>. In other fields, Raman spectroscopy has been used to, e.g., detect counterfeit medicines, identify plastic types in recycling flows, to detect hazardous chemicals, or to measure temperature<sup>5-9</sup>. Raman spectrum provides a fingerprint of the material, but it is usually not possible to directly interpret e.g. the material composition from the spectrum. In order to use Raman in the above-mentioned material classification and identification applications, a database of known reference spectra is needed. To this end, databases of experimental spectra have been collected, such as the RRUFF Project<sup>10</sup> that contains a large set of experimental Raman spectra of minerals (4112 public samples), KnowItAll Raman Spectral Library<sup>11</sup> that include Raman spectra of different organic and inorganic compounds, polymers and monomers (over 25000 records), and Raman Open Database(ROD)<sup>12</sup> which complements the crystallographic information found in the Crystallographic Open Database (COD)<sup>13</sup> (1133 entries).

A Raman Spectrum database made via ab initio, density-functional theory (DFT) electronic structure calculations could be highly useful in providing supplementary information that is difficult to obtain from experiments. For instance, some materials can be difficult to synthesize in a pure form, or their purity or phase content is unknown. The calculated results are also free of any instrumental contributions. Computational studies can also be faster and cheaper to carry out than experiments. Such a database would also be useful to computational researchers, e.g., by providing a reference spectra. Moreover, large datasets can be used in material informatics for material screening or for training models via machine-learning. Still, compared to the experimental ones, the computational databases are of very limited size. This is due to the computational cost of these calculations, which makes them limited to small systems and/or a small number of materials. A few open-access libraries of computational Raman spectra already exist such as: (i) Computational 2D Materials Database (C2DB)<sup>9,14</sup> that contains properties of a large number of 2D materials but only 733 structures have Raman spectra, (ii) WURM project<sup>15</sup> is a database of computed Raman and infrared spectra for 461 minerals, and (iii) in developing high-throughput computational methods, Liang et al. calculated 55 inorganic compounds<sup>16</sup>.

In this paper, we report on our research to develop optimized high-throughput workflow to carry out these calculations and build a large database of computational Raman spectra. For selected systems, the calculated

spectra are compared to those obtained using previous computational methods as well as to the experimental ones reported in the literature. The database of Raman spectra and vibrational properties reported along with this paper consists of 5099 compounds from many different material classes, far surpassing in size the previous computational databases and comparable to the experimental ones.

## Methods

### Simulation of Raman spectra

In Raman spectroscopy measurements, incident laser photons with a specific frequency  $\omega_L$  interact with lattice vibrations, described in the form of phonons in crystalline materials, and the spectrum of inelastically scattered photons are recorded. Scattered photons exhibit either a decrease in frequency  $\omega_S$  upon creation of phonon or increase in frequency upon annihilation of a phonon, denoted as Stokes or Anti-Stokes shifts, respectively. The intensity of the peaks is related to the Raman scattering cross section, which can be challenging to calculate since the ion (and electron) dynamics in the material need to be described concurrently with the light-matter interaction<sup>17,18</sup>.

There are several approaches for calculating the Raman spectra: (i) scattering probability from third-order perturbation theory (absorption, electron-phonon coupling, and emission)<sup>9,19,20</sup>, (ii) from the gradient of the electronic susceptibility (usually via finite-differences) in Placzek approximation<sup>20-22</sup>, and (iii) from the auto-correlation function of time-dependent susceptibility<sup>23,24</sup>. Methods (i) and (ii) only yield the Raman tensor, but the phonon eigenvectors and frequencies need to be determined first in a separate calculation step. In method (iii), the peak positions and intensities are obtained at once, but it is computationally highly demanding. Method (ii) is computationally most affordable and easy to implement in high-throughput setting<sup>16</sup> and thus adopted in this work. The method is briefly described below.

In the first step, the phonons are calculated as described in depth in many previous publications<sup>25,26</sup>. Within harmonic approximation, the potential energy surface is written as a Taylor expansion  $U = U_0 + \Phi_{\alpha\beta}(ki, lj)u_\alpha(ki)u_\beta(lj)$ , where  $U_0$  is the ground state energy and force constant matrix  $\Phi$  describes the second-order change in potential energy,

$$\Phi_{\alpha\beta}(ki, lj) = \frac{\partial^2 U}{\partial u_\alpha(ki) \partial u_\beta(lj)} = \frac{\partial F_\alpha(ki)}{\partial u_\beta(lj)} \quad (1)$$

In Eq. (1),  $u_\alpha(ki)$  is the displacement of the  $k$ th atom in the  $i$ th unit cell in the cartesian direction  $\alpha$ .  $F_\alpha(ki)$  is the force in atom  $ki$ , and in the equation above its change is induced by the displacement of atom  $lj$ . After harmonic ansatz for the temporal evolution of the vibrational modes  $v$ , the classical equations of motion for atoms in unit cell "0" become

$$M_k \omega^2 v_\alpha(k0) = \sum_{l,j,\beta} \Phi_{\alpha,\beta}(k0, lj) v_\beta(lj) \quad (2)$$

where  $M_k$  is the mass of atom  $k$ . The infinite sums over unit cells  $l$  in periodic crystals can be avoided by moving to reciprocal space and, after rescaling  $v$  and  $\Phi$  by  $\sqrt{M}$ , Eq. 2 is cast into an eigenvalue equation

$$\sum_{l\beta} D_{\alpha\beta}(kl, q) e_\beta(l, qv) = [\omega(qv)]^2 e_\alpha(k, qv) \quad (3)$$

where  $D$  is the mass-scaled Fourier-transformed  $\Phi$  (denoted dynamical matrix),  $q$  is the wave vector,  $e$  is the eigenvector of the band index  $v$ , and  $\omega^2$  are the eigenvalues. To obtain  $D$ , force constants  $\Phi$  need to be evaluated from the forces induced at atoms  $lj$  by displacing each atom  $k0$  in the unit cell. To guarantee sufficiently large distance between atoms  $k0$  and  $lj$ , supercell calculations are usually required. If the crystal symmetry is not considered, the construction of the force constant matrix requires performing  $3N$  DFT calculations when each of the  $N$  atoms in the unit cell is displaced in each of the three cartesian directions.

Differential cross section for the Stokes component of Raman scattering from the  $v$ th eigenmode far from resonance is given as<sup>17,22</sup>

$$\frac{d\sigma_v}{d\Omega} = \frac{\omega_S^4 V^2}{(4\pi)^2 c^4} \left| \hat{E}_S \frac{\partial \chi}{\partial \xi_v} \hat{E}_L \right|^2 \frac{\hbar(n+1)}{2\omega_v} \quad (4)$$

where  $\hat{E}_S$  and  $\hat{E}_L$  are the unit vectors of the polarization for the scattered and the incident light,  $V$  is scattering volume, and  $\xi$  is a normal-mode coordinate along the mass-scaled eigenvector  $e'_\alpha(k) = e_\alpha(k)/\sqrt{M_k} \sim v_\alpha(k)$  and  $\chi$  is the electronic susceptibility tensor. The directional derivative can be written out as

$$\frac{\partial \chi}{\partial \xi} = \nabla \chi \cdot e' = \sum_k^{unitcell} \frac{\partial \chi}{\partial u_\alpha(k)} M_k^{-\frac{1}{2}} e_\alpha(k) \approx \frac{\chi(R_0 + h'e') - \chi(R_0 - h'e')}{2h'} = \frac{\chi(R_0 + h\hat{e}') - \chi(R_0 - h\hat{e}')}{2h} |e'| \quad (5)$$

The first two forms involve calculation of derivatives of  $\chi$  with respect to displacement of each atom  $u(k)$ , whereas in the last two forms all atoms are displaced simultaneously along  $e'$  and explicitly written in the finite-difference approximation as implemented in the code (displacing the atoms in both positive and negative directions). Normalized  $\hat{e}' = e'/|e'|$  (and  $h = h'|e'|$ ) is used in order to have consistent step size  $h$  in systems and modes with different masses (and in units of Å).

Specifically, the Raman tensor is defined as<sup>22</sup>

$$R_{\nu\beta\gamma} = \frac{V_c}{4\pi} \frac{\partial \chi_{\beta\gamma}}{\partial \xi_\nu} \quad (6)$$

incorporating  $V^2/(4\pi)^2$  from Eq. (4). To evaluate the change in  $\chi$ , we used the macroscopic dielectric constant  $\epsilon_{\beta\gamma}$  containing only the electronic contribution with clamped ions (sometimes denoted as the high-frequency dielectric constant  $\epsilon_\infty$ ), which is readily provided by most DFT codes.

While the expression in Eq. (4) yields complete information, quite often experimental results are obtained for polycrystalline mineral specimens or powdered samples, in which case the intensity must be averaged over all possible orientations of the crystals. When the direction of incident light, its polarization, and the direction of outgoing light are all perpendicular, the Raman intensity becomes<sup>20,22</sup>

$$\frac{d\sigma_\nu}{d\Omega} = \frac{\omega_S^4}{c^4} \frac{\hbar(n+1)}{2\omega_\nu} \frac{I_{\text{Raman}}}{45} \quad (7)$$

where

$$I_{\text{Raman}} = 45a^2 + 7\gamma^2 \quad (8)$$

$$a = \frac{1}{3}(R_{vxx} + R_{vyy} + R_{vzz}) \quad (9)$$

$$\gamma^2 = \frac{1}{2}[(R_{vxx} - R_{vyy})^2 + (R_{vxx} - R_{vzz})^2 + (R_{vyy} - R_{vzz})^2 + 6(R_{vxy}^2 + R_{vzx}^2 + R_{vyz}^2)] \quad (10)$$

$I_{\text{Raman}}$  is Raman activity that is independent of experimental factors such as temperature and incoming photon energy and thus used when comparing our results to other calculations, whereas Eq. 7 is used (and must be used) when comparing to experimental spectra.

## Workflow

We now describe how the theory described above is turned to an efficient computational workflow. As mentioned, the computational procedure involves two sets of calculations: (i) force constants to get the vibrational modes and (ii) the Raman tensors for each mode. While the phonons at  $\Gamma$ -point can be calculated efficiently, we would like to have access to the full force constant matrix. This allows calculation of phonon dispersion and also, e.g., estimation of isotope effects and line broadening due to defects or grains via phonon confinement model<sup>17,27–29</sup>. Both steps can be computationally demanding for systems with large number of atoms in the unit cell, which has hindered previous efforts to building such databases in the past.

The most important design decisions that distinguish our work from the previous ones are the following. First, we have decided to build our database on top of the Atsushi Togo's Phonon database<sup>30</sup>, that contains the calculated full force constant matrix, and our work only focuses on calculating the Raman tensors. We are using the same computational parameters, and thus our database is fully consistent with the Phonon database, which is further linked to the Materials project database<sup>31</sup> via the material-IDs.

Second, to reduce calculation time and make the workflow more efficient compared to existing methods, Raman-active modes are found based on group theory and the Raman tensors are calculated only for modes that are known to be active or whose activity could not be determined. Known inactive modes and the three zero-frequency acoustic modes are ignored. For this purpose, the symmetry information about Raman activity was implemented.

The workflow developed for automatic Raman tensors calculations is illustrated in Fig. 1. At the conceptual level, the workflow steps are following:

1. Select material from Phonon database, read in optimized structure, computational parameters, and force constant matrix.
2. Calculate the eigenvectors and eigenvalues at  $\Gamma$ -point.
3. Determine the irreducible representation (irrep) of the modes and whether they are Raman and/or infrared active.
4. Perform prescreening to check that the material is dynamically and thermodynamically stable and the material is not metallic or near-metallic.
5. Calculate the Raman tensors for Raman-active modes and the dielectric tensors for the optimized structure.
6. All the results (structure, eigenvalues, irreducible representation, Raman tensors, etc.) are collected in a database.

The softwares used in each step are also indicated in Fig. 1. Atsushi Togo's Phonon database contains the optimized structures, calculated force constants, and all the computational parameters used to obtain them. These are calculated using VASP software<sup>32,33</sup>. The eigenvalues and eigenvectors at  $\Gamma$ -point, as well as the irreducible representations of the modes are calculated using Phonopy<sup>30</sup>. All of this information together with selected material properties obtained from the Materials Project database are collected in a database for prescreening. For this, we adopted to use the database tools in atomic simulation environment (ASE)<sup>34</sup>. In the last step, the calculated Raman tensors are added to this database, which is then also served through a web app implemented in ASE.

For automating the computationally intensive part, i.e., the calculation of the Raman tensors, we used the Atomate<sup>35</sup> that is a Python-based package for constructing complex materials science computational workflows. The workflow objects generated by Atomate are given to Fireworks workflow software<sup>36</sup> for managing, storing, and executing them with the help of Custodian package for error management<sup>37</sup>. As the DFT calculator we used here VASP, with the parameters taken from the Phonon database. During these calculations, all the input parameters and results are stored in a Mongo database, which are afterwards transferred to the database (Computational Raman Database, CRD).

### Prescreening

Before Raman tensor calculations we performed the following prescreening, also illustrated in Fig. 2: (i) We check that the material has Raman active mode(s) based on the symmetry analysis. (ii) We check that the material is dynamically stable, i.e., there are no modes with imaginary frequencies at the  $\Gamma$ -point. (iii) We check that the material is thermodynamically stable by requiring that the energy above the convex hull is less than 0.1 eV/atom, as materials with the energy  $> 0.1$  eV are unlikely to be experimentally synthesized<sup>38</sup>. (iv) We check that the bandgap is larger than 0.5 eV, since our computational approach is strictly valid only for non-resonant conditions (i.e., photon energy smaller than the band gap), and metallic systems require very large k-point meshes which will increase the computational cost. For (iii) and (iv) we use information from the Materials Project database at the same material ID<sup>31</sup>. Finally, we have 8382 (83.55%) materials satisfying these conditions and flagged for calculation. It is also worth noting that Phonon database contains only materials that are non-metallic, non-magnetic, and non-triclinic.

The workflow first performs calculation of dielectric tensors of the optimized structure, which can be compared to that provided in Phonon database. Additionally, the maximum forces are checked in this step and the calculation terminated if the forces are  $> 0.001$  eV/ $\text{\AA}$ , but no such case was encountered.

### Computational parameters

All density-functional theory (DFT) calculations are carried out using VASP (Vienna Ab initio Simulation Package)<sup>32,39</sup> with projector-augmented wave method<sup>40</sup>. PBEsol exchange-correlation functional<sup>41</sup> and other computational parameters were taken to be the same as used in Phonon database. In particular, plane wave cutoff is set to 1.3 times the maximum cutoff listed in PAW setups. In Phonon database, the structures of standardized unit cells are given, whereas we adopt to use the primitive cell in Raman tensor calculations to save computational time. The primitive cell can be readily obtained using Phonopy<sup>30</sup>. In the calculation of eigenvectors, non-analytic corrections are not included, as the eigenvectors would then depend also on the direction from which  $q \rightarrow 0$  is approached and thereby complicate the calculations significantly. Fortunately, this mostly happens for the IR-active modes and less

for the Raman-active modes. Moreover, the induced change in eigenvectors and in Raman tensors is expected to be small and the splitting of the modes can be determined a posteriori.

There are then only two parameters left to decide: the k-point mesh and the magnitude of the atomic displacements in evaluation of the Raman tensor by finite differences.

In Phonon database, the Brillouin zone of the unit cell is sampled by a mesh whose density is defined by the  $R_k$  parameter in VASP. We adopt the same approach, but it is worth noting that since we use primitive cell, the exact density and positions of mesh points can be slightly different. Moreover, metals and small-gap semiconductors usually require higher density k-point mesh than large-gap insulators. All calculations in the Phonon database used  $R_k = 20$ , which should be sufficient for the structural optimization of materials included in the database (band gap  $> 0.5$  eV). Determination of Raman tensor may, however, require a higher value. In order to benchmark this, we selected two materials from the Phonon database with different band gaps: the largest band gap material among the common III-V semiconductors is AlN (4.05 eV) and Si is a small band gap material (0.85 eV).

As illustrated in Fig. S1,  $R_k = 40$  is needed to achieve converged results for dielectric constant and Raman intensity of a small band gap material Si, whereas for a large band gap material AlN  $R_k = 20$  is sufficient. See Benchmark section in SI for more details. In our workflow, we have chosen to use the following values:  $R_k = 20$  for the structures with a band gap more than the 2 eV,  $R_k = 30$  for band gaps in the range of 1–2 eV, and  $R_k = 40$  for band gaps smaller than 1 eV.

In order to benchmark the displacement, we chose materials with heavy and light elements, PbO and Cd(HO)<sub>2</sub>. As shown in Fig. S2, varying the displacement from 0.001 Å to 0.04 Å (default value being 0.005 Å), we found little change in the Raman tensors or the dielectric constants. Therefore, we chose to use the default value. Finally, we verified the computational workflow in Atomate by comparing the Raman spectra of few structures to those obtained using VASP\_Raman code<sup>42</sup>. As shown in Fig. S3, a good agreement is found. We note that Atomate had wrong normalization of eigenvectors which in some cases resulted in overestimation of the Raman intensities, but was fixed in the version used here.

## Data Records

### Computational Raman Database

The final database contains vibrational information and Raman tensors stored in JSON document that can be downloaded directly from the Materials Cloud Archive<sup>43</sup> and queried with a simple python script. The Table 1 shows all the database keys with their related descriptions. The data can also be browsed online in Computational Raman Database website ([ramandb.oulu.fi](http://ramandb.oulu.fi)).

### Database statistics

As shown in Fig. 2, there were 10032 materials in the Phonon database and 8382 of them were flagged for calculation. Since each structure contains several vibrational modes, the total number of modes in our database was 725163, and 428081 modes of them are Raman active or the activity is unknown.

Figs. 3(a,b) shows the number of materials in the database (before prescreening) grouped by the calculated band gaps and the number of atoms in their structures, respectively. The histogram with respect to the number of atoms, peaks at around 20–30. There are some materials with very large primitive cells containing more than 100 atoms, but many of these appear to be disordered/alloyed/defective variants of the small primitive cell systems and thus of limited interest. Since the Phonon database only includes non-metallic materials, the number of materials with a band gap smaller than 0.5 eV is small, and therefore neglecting those materials in our prescreening step has small impact.

We proceeded to carry out the Raman tensor calculations in the order of increasing number of atoms in the primitive cell. The database included here contains 5099 calculated structures. We calculated all materials with less than 10 atoms in the primitive cell and all experimentally observed materials (as indicated by MP) less than 40 atoms in the primitive cell. For this, we used about 9.5 million CPU hours. We estimate that for calculating the remaining 3283 structures would require more than 20 million CPU hours, owing to the much larger cell sizes.

In Fig. 3(c) we compare the number of materials considered in this work and in Materials Project database as grouped by the type of compound (oxides, halides, etc.). "MP" denotes the full Materials Project database, whereas "MP\*" includes the same conditions (band gap larger than 0.5 eV and energy above hull less than 0.1 eV) as used in our material set (PhDB\*). "CRD" refers to the calculated set of materials. In total, almost 20% of the MP\* structures are contained in the PhDB\* dataset and about 12% are calculated. Also, the different types of compounds are included in our database with similar statistics as in Materials Project. As an example, the percentage of oxides and halogenides are 52 % and 27 % in our database, compared to 67 % and 26 % in MP\*. Finally, we used the algorithm



proposed by Larsen et al.<sup>44</sup> for identifying the dimensionality of the structures in our database: 4137 structures (more than 80 %) are three-dimensional, 385 structures are two-dimensional, 72 structures are one-dimensional, 277 structures are 0D and others are a mixture of different dimensionality, such as 0D+1D, 0D+2D, 0D+3D, etc. This shows that our database covers most different material classes.

## Technical Validation

### Comparison to experiments

Selected computational benchmarks were already presented in the Computational parameters section. In this section, we compare the calculated spectra from our approach with experimental results extracted from the RRUFF database to validate our method and calculations. RRUFF contains only (estimated) chemical formula and lattice parameters but not atomic positions, and thus we cannot guarantee exact structural match. Based on mineral names, there are 703 entries in RRUFF database that matched with 288 structures of our database. The Table S1 contains mineral names, formula, and their RRUFF IDs for structures with the same formula as found in Phonon database, 92 in total. 27 of these were found to have the similar lattice parameters compared to the matched structure in our database and thus very likely to be the same structure. Moreover, in most cases, the energy above hull is zero or very small, the maximum being 40 meV/atom.

Fig. 4 shows a comparison between calculated spectra and experimental Raman spectra of few selected minerals: HgO, MgCO<sub>3</sub>, CaMg(CO<sub>3</sub>)<sub>2</sub>, and SiO<sub>2</sub>. Overall good agreement between computational and experimental results is found. In most cases, the frequencies (Raman shifts) differ from the experimental values by less than few percent. The variation in peak intensities is somewhat larger but qualitatively correct. We note that the comparison to the experiment is complicated by the varying linewidths in the experimental spectra, which in turn modifies the peak maxima. The linewidth is related to the phonon lifetime, which is not evaluated in our calculations. Instead, in the simulated spectra we have only included a reasonable phonon lifetime-induced broadening of 8 cm<sup>-1</sup>. The experimental spectra appear to contain also a Gaussian-type (instrumental) broadening, which we do not attempt to reproduce here. Also, while perfectly ordered bulk crystals are used in calculations, in experiments the material purity or even exact composition may be unknown and the spectrum is affected by parameters such as temperature, pressure, and measurement geometry. While we are relying in harmonic approximation, phonon renormalization due to anharmonic effects can affect the frequencies as well as linewidths. Also, we are simulating non-resonant Raman spectra, while in resonant Raman the intensities may change depending on the electronic resonance conditions. Nevertheless, in the cases where the Raman tensors are affected by any of these effects, the Raman-active modes found based on the group theory can still be used to assist in the analysis of the experimental spectra.

## Usage Notes

We introduced an optimized workflow for performing high-throughput first-principles calculations of Raman tensors. The workflow takes full advantage of the crystal symmetry, adopts carefully benchmarked computational parameters, and avoids calculation of vibrational modes by importing them from existing Phonon database. We carried out such calculations for 5099 materials and the results are included in the dataset accompanying this paper. The database encompasses a wide variety of materials from different compound classes (oxides, halides, etc.) and of different dimensionality. The calculated spectra were also shown to compare favorably with the experimental ones.

The final database contains Raman tensors and other vibrational information, such as phonon eigenmodes, Born charges, and symmetry information, stored in JSON document that can be downloaded directly from the Materials Cloud Archive<sup>43</sup> and queried with a simple python script. The whole dataset can also be browsed online in Computational Raman Database website (<http://ramandb.oulu.fi>), wherein one can also find other relevant information, such as atomic structure, phonon dispersion, and infrared spectrum. We hope that the vibrational properties and Raman spectra of materials in the database will prove useful for computational and experimental researchers alike.

## Code availability

VASP<sup>32,33</sup> used in all DFT calculations is a proprietary software. For the database, dimensionality analysis, and web app, we used Atomic Simulation Environment (ASE)<sup>34</sup>, released under GNU Lesser General Public License (LGPL). Phonopy<sup>30</sup> used in calculating the eigenvectors and performing symmetry analysis is released under New Berkeley Software Distribution (BSD) License. The workflow is defined as a part of Atomate code package<sup>35</sup> with

FireWorks<sup>36</sup> for defining, managing, and executing jobs which both are released under a modified BSD license and free to the public. Pymatgen (Python Materials Genomics) used for producing inputs parameters and custodian<sup>37</sup> for performing error checking are both open-source packages under Massachusetts Institute of Technology (MIT) license. To store results and task parameters, MongoDB NoSQL database was used with the Server Side Public License (SSPL). All the information for prescreening and phonon calculation extracted from Phonon Database<sup>30,45</sup> and from Materials project<sup>31,46</sup> are both released under Creative Commons Attribution 4.0 International License.

## References

1. Das, R. S. & Agrawal, Y. Raman spectroscopy: Recent advancements, techniques and applications. *Vib. Spectrosc.* **57**, 163–176, <https://doi.org/10.1016/j.vibspec.2011.08.003> (2011).
2. Schrader, B. *Infrared and Raman spectroscopy: methods and applications* (John Wiley & Sons, 1995).
3. Parker, F. S. *Applications of infrared, Raman, and resonance Raman spectroscopy in biochemistry* (Springer Science & Business Media, 1983).
4. Vašková, H. A powerful tool for material identification: Raman spectroscopy. *Int. J. Math. Model. Methods Appl. Sci* **5**, 1205–1212 (2011).
5. Scotter, C. N. Non-destructive spectroscopic techniques for the measurement of food quality. *Trends Food Sci. & Technol.* **8**, 285–292, [https://doi.org/10.1016/S0924-2244\(97\)01053-4](https://doi.org/10.1016/S0924-2244(97)01053-4) (1997).
6. Bicchieri, M., Sodo, A., Piantanida, G. & Coluzza, C. Analysis of degraded papers by non-destructive spectroscopic techniques. *J. Raman Spectrosc.* **37**, 1186–1192, <https://doi.org/10.1002/jrs.1603> (2006).
7. Orlando, A. *et al.* A comprehensive review on raman spectroscopy applications. *Chemosensors* **9**, 262, <https://doi.org/10.3390/chemosensors9090262> (2021).
8. Adya, A. K. & Canetta, E. Nanotechnology and its applications to animal biotechnology. In *Animal Biotechnology*, 309–326, <https://doi.org/10.1016/b978-0-12-811710-1.00014-8> (Elsevier, 2020).
9. Taghizadeh, A., Leffers, U., Pedersen, T. G. & Thygesen, K. S. A library of ab initio Raman spectra for automated identification of 2D materials. *Nat. Commun.* **11**, 1–10, <https://doi.org/10.1038/s41467-020-16529-6> (2020).
10. Lafuente, B., Downs, R. T., Yang, H. & Stone, N. *The power of databases: The RRUFF project* (De Gruyter, 2016).
11. Knowitall raman spectral database collection. <https://sciencesolutions.wiley.com/>. Accessed: 2022-08-23.
12. El Mendili, Y. *et al.* Raman Open Database: first interconnected Raman–X-ray diffraction open-access resource for material identification. *J. Appl. Crystallogr.* **52**, 618–625, <https://doi.org/10.1107/S1600576719004229> (2019).
13. Gražulis, S. *et al.* Crystallography Open Database – an open-access collection of crystal structures. *J. Appl. Crystallogr.* **42**, 726–729, <https://doi.org/10.1107/S0021889809016690> (2009).
14. Haastrup, S. *et al.* The computational 2d materials database: high-throughput modeling and discovery of atomically thin crystals. *2D Mater.* **5**, 042002, <https://doi.org/10.1088/2053-1583/aacfc1> (2018).
15. Caracas, R. & Bobocioiu, E. The WURM project—a freely available web-based repository of computed physical data for minerals. *Am. Mineral.* **96**, 437–443, <https://doi.org/10.2138/am.2011.3532> (2011).
16. Liang, Q., Dwaraknath, S. & Persson, K. A. High-throughput computation and evaluation of raman spectra. *Sci. Data* **6**, 1–7, <https://doi.org/10.1038/s41597-019-0138-y> (2019).
17. Cardona, M. Resonance phenomena. In *Topics in Applied Physics*, Topics in applied physics, 19–178 (Springer Berlin Heidelberg, Berlin, Heidelberg, 1982).
18. Reichardt, S. & Wirtz, L. Theory of resonant raman scattering: Towards a comprehensive ab initio description. *Phys. Rev. B* **99**, 174312, <https://doi.org/10.1103/PhysRevB.99.174312> (2019).
19. Lee, S. & Heller, E. J. Time-dependent theory of raman scattering. *The J. Chem. Phys.* **71**, 4777–4788, <https://doi.org/10.1063/1.438316> (1979).
20. Long, D. A. *The Raman effect* (John Wiley & Sons, Chichester, England, 2002).
21. Placzek, G. *Rayleigh-streuung und Raman-effekt*, vol. 2 (Akademische Verlagsgesellschaft, 1934).
22. Porezag, D. & Pederson, M. R. Infrared intensities and Raman-scattering activities within density-functional theory. *Phys. Rev. B - Condens. Matter Mater. Phys.* **54**, 7830–7836, <https://doi.org/10.1103/PhysRevB.54.7830> (1996).

23. Gordon, R. Correlation functions for molecular motion. In WAUGH, J. S. (ed.) *Advances in Magnetic Resonance*, vol. 3 of *Advances in Magnetic and Optical Resonance*, 1–42, <https://doi.org/10.1016/B978-1-4832-3116-7.50008-4> (Academic Press, 1968).
24. Thomas, M., Brehm, M., Fligg, R., Vöhringer, P. & Kirchner, B. Computing vibrational spectra from ab initio molecular dynamics. *Phys. Chem. Chem. Phys.* **15**, 6608–6622, <https://doi.org/10.1039/C3CP44302G> (2013).
25. Yu, P. Y. & Cardona, M. *Fundamentals of Semiconductors* (Springer Berlin Heidelberg, 2010).
26. Baroni, S., de Gironcoli, S., Dal Corso, A. & Giannozzi, P. Phonons and related crystal properties from density-functional perturbation theory. *Rev. Mod. Phys.* **73**, 515–562, <https://doi.org/10.1103/RevModPhys.73.515> (2001).
27. Hashemi, A., Krasheninnikov, A. V., Puska, M. & Komsa, H.-P. Efficient method for calculating raman spectra of solids with impurities and alloys and its application to two-dimensional transition metal dichalcogenides. *Phys. Rev. Mater.* **3**, 023806, <https://doi.org/10.1103/PhysRevMaterials.3.023806> (2019).
28. Kou, Z., Hashemi, A., Puska, M. J., Krasheninnikov, A. V. & Komsa, H.-P. Simulating raman spectra by combining first-principles and empirical potential approaches with application to defective MoS<sub>2</sub>. *npj Comput. Mater.* **6**, <https://doi.org/10.1038/s41524-020-0320-y> (2020).
29. Gillet, Y., Kontur, S., Giantomassi, M., Draxl, C. & Gonze, X. Ab initio approach to second-order resonant raman scattering including exciton-phonon interaction. *Sci. Reports* **7**, <https://doi.org/10.1038/s41598-017-07682-y> (2017).
30. Togo, A. & Tanaka, I. First principles phonon calculations in materials science. *Scripta Materialia* **108**, 1–5, <https://doi.org/10.1016/j.scriptamat.2015.07.021> (2015).
31. Jain, A. *et al.* The Materials Project: A materials genome approach to accelerating materials innovation. *APL Mater.* **1**, 011002, <https://doi.org/10.1063/1.4812323> (2013).
32. Kresse, G. & Furthmüller, J. Efficiency of ab-initio total energy calculations for metals and semiconductors using a plane-wave basis set. *Comput. Mater. Sci.* **6**, 15–50, [https://doi.org/10.1016/0927-0256\(96\)00008-0](https://doi.org/10.1016/0927-0256(96)00008-0) (1996).
33. Kresse, G. & Joubert, D. From ultrasoft pseudopotentials to the projector augmented-wave method. *Phys. Rev. B* **59**, 1758–1775, <https://doi.org/10.1103/PhysRevB.59.1758> (1999).
34. Larsen, A. H. *et al.* The atomic simulation environment—a python library for working with atoms. *J. Physics: Condens. Matter* **29**, 273002, <https://doi.org/10.1088/1361-648x/aa680e> (2017).
35. Ceriotti, M., Pietrucci, F. & Bernasconi, M. Ab initio study of the vibrational properties of crystalline TeO<sub>2</sub>: The  $\alpha$ ,  $\beta$ , and  $\gamma$  phases. *Phys. Rev. B - Condens. Matter Mater. Phys.* **73**, 1–17, <https://doi.org/10.1103/PhysRevB.73.104304> (2006).
36. Jain, A. *et al.* Fireworks: a dynamic workflow system designed for high-throughput applications. *Concurr. Comput. Pract. Exp.* **27**, 5037–5059, <https://doi.org/10.1002/cpe.3505> (2015).
37. Ong, S. P. *et al.* Python materials genomics (pymatgen): A robust, open-source python library for materials analysis. *Comput. Mater. Sci.* **68**, 314–319, <https://doi.org/10.1016/j.commatsci.2012.10.028> (2013).
38. Sun, W. *et al.* The thermodynamic scale of inorganic crystalline metastability. *Sci. Adv.* **2**, e1600225, <https://doi.org/10.1126/sciadv.1600225> (2016).
39. Kresse, G. & Furthmüller, J. Efficient iterative schemes for ab initio total-energy calculations using a plane-wave basis set. *Phys. Rev. B* **54**, 11169–11186, <https://doi.org/10.1103/PhysRevB.54.11169> (1996).
40. Blöchl, P. E. Projector augmented-wave method. *Phys. Rev. B* **50**, 17953–17979, <https://doi.org/10.1103/PhysRevB.50.17953> (1994).
41. Perdew, J. P. *et al.* Restoring the density-gradient expansion for exchange in solids and surfaces. *Phys. Rev. Lett.* **100**, 136406, <https://doi.org/10.1103/PhysRevLett.100.136406> (2008).
42. Fonari, A. & Stauffer, S. *vasp\_raman.py* (<https://github.com/raman-sc/VASP/>, 2013).
43. Bagheri, M. & Komsa, H.-P. High-throughput computation of raman spectra from first principles. *Mater. Cloud Arch.* **2022.104** <https://doi.org/10.24435/materialscloud:ze-58> (2022).
44. Larsen, P. M., Pandey, M., Strange, M. & Jacobsen, K. W. Definition of a scoring parameter to identify low-dimensional materials components. *Phys. Rev. Mater.* **3**, 034003, <https://doi.org/10.1103/PhysRevMaterials.3.034003> (2019).



45. Hinuma, Y., Pizzi, G., Kumagai, Y., Oba, F. & Tanaka, I. Band structure diagram paths based on crystallography. *Comput. Mater. Sci.* **128**, 140–184, <https://doi.org/10.1016/j.commatsci.2016.10.015> (2017).
46. Ong, S. P. *et al.* The materials application programming interface (API): A simple, flexible and efficient API for materials data based on REpresentational state transfer (REST) principles. *Comput. Mater. Sci.* **97**, 209–215, <https://doi.org/10.1016/j.commatsci.2014.10.037> (2015).

## Acknowledgements

We thank CSC-IT Center for Science Ltd. for generous grants of computer time. Also, We acknowledge discussions with Prof. Atsushi Togo on the details concerning the Phonon database

## Author contributions statement

## Competing interests

The authors declare no conflict of interest.

## Figures & Tables

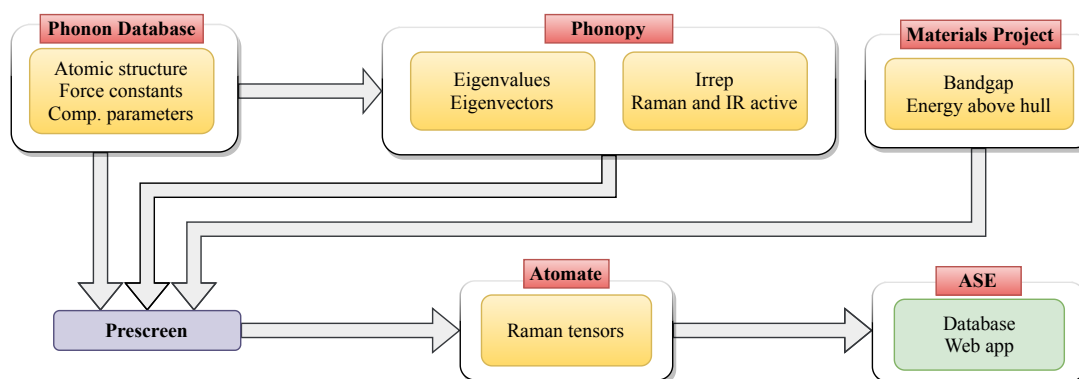


**Figure 1.** High-throughput calculation workflow, grouped according to the software or database used (red box) and the light yellow boxes indicating the relevant material properties.

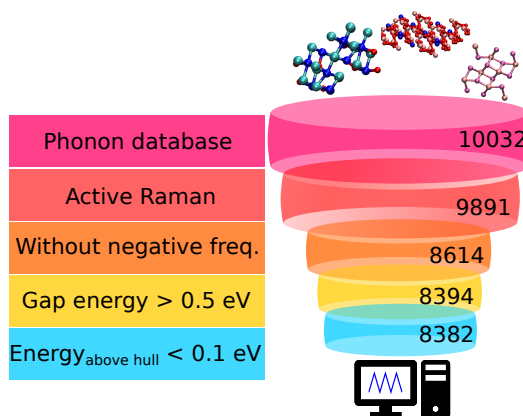


**Figure 2.** Structure selection procedure. The prescreening criteria are indicated on the left and the the number of structures in each step are indicated on the right.

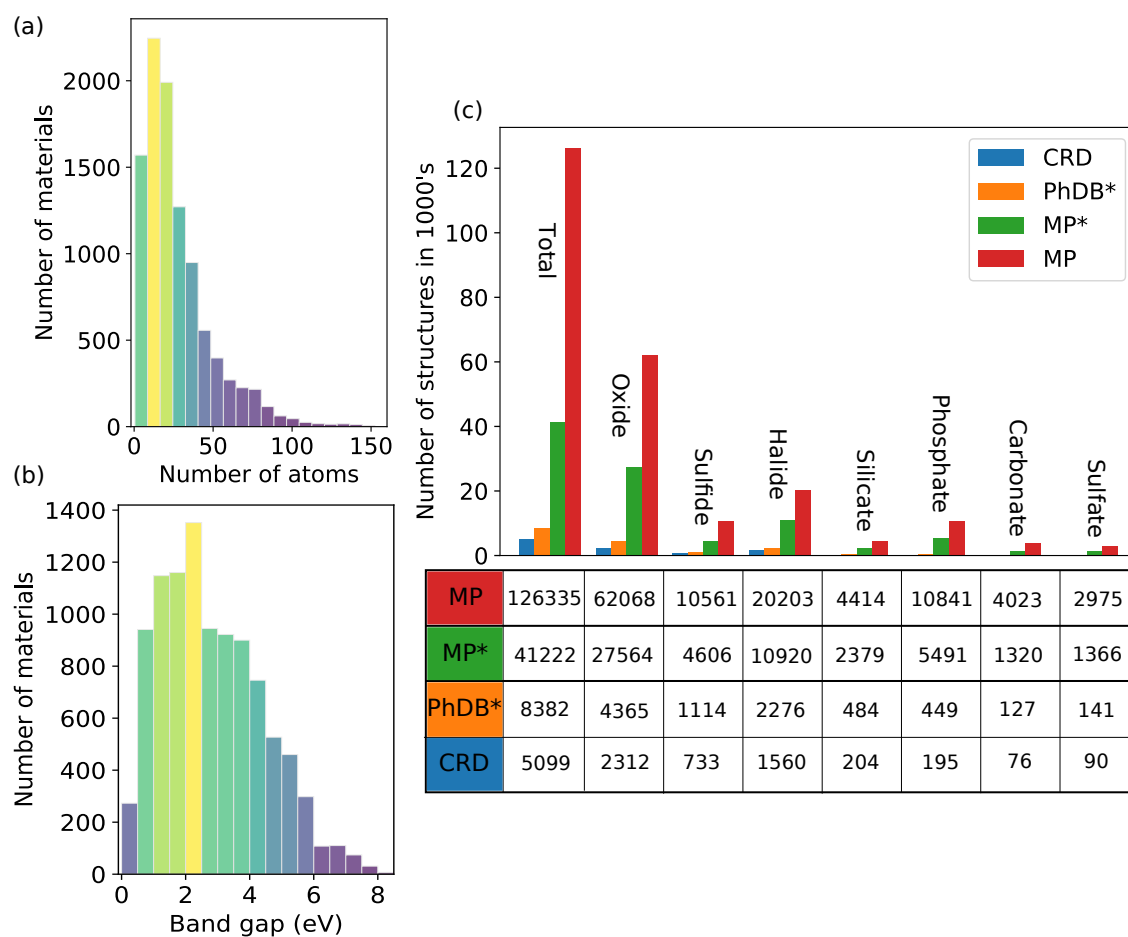


**Figure 3.** Database statistics. (a), (b) The number of materials in Phonon database as a function of number of atoms in structures and band gap, respectively. (c) Comparison of the number of different types of compounds in Material Project (MP) and Computational Raman Database (CRD). MP\* and PhDB\* shows the number of structures in Materials Project and Phonon database, respectively, when the same selection conditions as in CRD are applied to them.

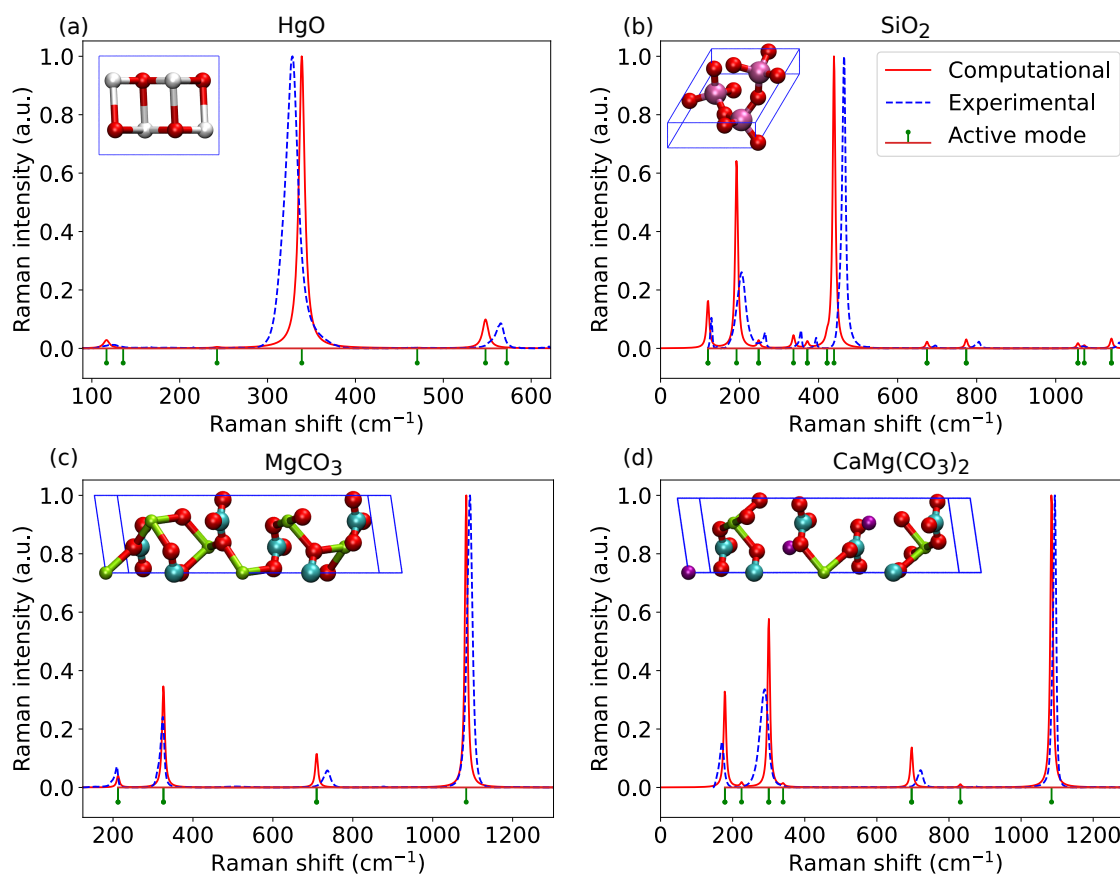


**Figure 4.** Comparison of calculated Raman spectra (red solid line) and experimental spectra from RRUFF database<sup>10</sup> (blue dashed line) for selected minerals. Green short line segments show the Raman active modes based on the symmetry analysis. Both spectra are normalized to one at maximum. The experimental spectra correspond to processed data measured at wavelength 532 nm from unoriented samples with RRUFF id: R140877, R050125, R050676, and R050129, for HgO, SiO<sub>2</sub>, MgCO<sub>3</sub>, and CaMg(CO<sub>3</sub>)<sub>2</sub>, respectively. The atomic structures are given in the inset (O: red, Hg: white, Si: magenta, Mg: green, C: cyan, Ca: purple).

Keys	Datatype	Description
lattice_parameters	list	$a$ , $b$ , and $c$ lattice constants ( $\text{\AA}$ )
lattice_angles	list	$\alpha$ , $\beta$ and $\gamma$ angles between lattice vectors
cell	array	Lattice vectors in $3 \times 3$ matrix format
positions	array	Atomic positions in relative coordinates
numbers	array	Total number of atoms and atomic numbers of all elements
mass	float	Sum of atomic masses in the unit cell (amu)
volume	float	Volume of the unit cell ( $\text{\AA}^3$ )
mpid	string	MP ID
bandgap_mp	float	Band gap from MP database (eV)
bandgap	float	Band gap (eV)
cbm	float	Conduction band minimum (eV)
vbm	float	Valence band maximum (eV)
diel_mp	array	Dielectric tensor (electronic contribution) from MP database
diel	array	Dielectric tensor (electronic contribution)
frequencies_thz	list	$\Gamma$ -point frequencies (THz)
frequencies_cm	list	$\Gamma$ -point frequencies ( $1/\text{cm}$ )
pointgroup	string	Point group
spacegroup	string	Space group
chemical_formula	string	Chemical formula
IRactive	array	Infrared-active modes
IRlabels	list	Irreducible representation (irrep) labels of modes
IRbands	list	Irrep. band groups of degenerate modes
natom	integer	Total number of atoms
Ramanactive	array	Raman activity of modes (0: inactive, 1: active, -1:unknown)
raman_tensors	array	Raman tensors
born	array	Born charges ( $e$ )
eigenvec	array	Eigenvectors
dimensionality	string	Dimensionality of structure
mp_e_above_hull	float	Energy above convex hull from MP database (eV/atom)
negative_freq_Gamma	boolean	Existence of negative frequencies at $\Gamma$ -point
negative_freq_path	boolean	Existence of negative frequencies in phonon dispersion
Refs	string	Links to Phonon database and MP websites

**Table 1.** Description of the JSON file structure for Computational Raman Database (CRD)

# Supplemental Material to "High-throughput computation of Raman spectra from first principles"

Mohammad Bagheri<sup>1</sup> and Hannu-Pekka Komsa<sup>1,\*</sup>

<sup>1</sup>Microelectronics Research Unit, Faculty of Information Technology and Electrical Engineering, University of Oulu, Oulu, FIN-90014, Finland

\*corresponding author(s): Hannu-Pekka Komsa (hannu-pekka.komsa@oulu.fi)

## ABSTRACT

### Benchmark

To benchmark of our approach, we selected four materials with different band gaps and different atomic masses: Si, PbO, AlN, and Cd(HO)<sub>2</sub>. We first verified that the standard approach of calculating Raman-tensors for all modes agrees with the Raman-active modes identified using group theory. That is, all the Raman-inactive modes were found to have vanishingly small Raman tensor, although often nonzero due to numerical errors.

Next, we investigated the effect of k-point mesh density on Raman tensors and Raman spectra. We calculated Raman tensors for  $R_k = 30, 40$  and  $60$  and compared the results with the standard value ( $R_k = 20$ ) used in Phonon database. Results from two (out of four) materials are shown in Fig. S1, where, to represent large and small bandgap materials, we selected AlN (4.05 eV) and Si (0.85 eV), respectively. Fig. S1(a,b) shows the unnormalized Raman activity spectra for different  $R_k$ , which clearly illustrates that AlN is hardly affected whereas Si experiences significant changes, thus suggesting that  $R_k$  should be increased. To better illustrate the magnitude of changes, Fig. S1(c,d) show how the maximum intensity changes with increasing  $R_k$  and Fig. S1(e,f) shows the average dielectric constant. In the case of AlN,  $R_k = 20$  already yields Raman tensors within 10 % of the converged value and dielectric constant within 1 %. In the case of Si,  $R_k = 40$  is required to reach similar accuracy. Based on these results we decided to use  $R_k=40$  for materials with bandgap smaller than 1 eV,  $R_k=30$  for materials with bandgap between 1 eV to 2 eV, and  $R_k=20$  for materials with a bandgap greater than 2 eV.

In the third step, we investigated the effect of step size by calculating Raman tensors of PbO and Cd(HO)<sub>2</sub> with step sizes of 0.001, 0.02, and 0.04 Å and compared them with those using the standard step size of 0.005 Å. Fig. S2 shows the changes in dielectric constants of PbO and Cd(HO)<sub>2</sub> in different directions and plotted for three-step sizes: 0.005, 0.02, and 0.04 Å. Since dielectric tensor is symmetric ( $xy=yx$ ,  $xz=zx$ , and  $yz=zy$ ), we only plot the inequivalent components. As shown in Fig. S2, whenever there are pronounced changes in the dielectric constant (corresponding to non-zero components in Raman tensor), the dependence on step size is close to linear. In some cases there is a small parabolic dependence, seen particularly well in the  $xy=yx$  component which contains no linear dependence, but these will not affect the Raman tensor since we are using two-point finite-difference stencil. Moreover, in this range of step sizes there is no discernible noise, although some noise could be observed in 0.001 Å results (not shown). Thus, we consider the default value of 0.005 Å a good choice.

As mentioned in the text, there was an error in the normalization of eigenvectors in Atomate. We fixed the normalization error and changed the formulations to match with the vasp\_raman code<sup>7,8</sup>. To verify our approach, we used vasp\_raman code to calculate Raman tensors and compared them to Atomate with the fixed and old versions of eigenvector normalization. Fig. S3 shows the Raman activity spectra of MoS<sub>2</sub>, WS<sub>2</sub>, SrGaSnH, and BaAlSiH. The revised normalization yields activities closely matching with vasp\_raman code. The incorrect normalization, on the other hand, tends to lead to overestimation of Raman activities and is particularly severe with modes that have very small Raman activity.

In CRD website ([ramandb.oulu.fi](http://ramandb.oulu.fi)), the total Raman intensity is separated into depolarized ( $I_{\perp}$ ) and polarized



( $I_{||}$ ) components,  $I = I_{\perp} + I_{||}$ , with

$$\frac{I_{||}}{(\omega_L - \omega_v)^4} \sim \frac{\hbar(n+1)}{30\omega_v} (10G_v^{(0)} + 4G_v^{(2)}) \quad (1)$$

$$\frac{I_{\perp}}{(\omega_L - \omega_v)^4} \sim \frac{\hbar(n+1)}{30\omega_v} (5G_v^{(1)} + 3G_v^{(2)}) \quad (2)$$

where we have taken out the  $(\omega_L - \omega_v)^4$  term that depends on the laser wavelength, since (i) this removes the dependence on one external parameter from our spectra, (ii) our calculations are for non-resonant conditions and one needs to be careful to only compare to wavelengths that are far from resonance, and (iii) the dependence on  $\omega_v$  and thus the changes in the spectra after normalization are usually small. The rotation invariants are<sup>?,?</sup>

$$G_v^{(0)} = \frac{1}{3} (R_{vxx} + R_{vyy} + R_{vzz})^2 \quad (3)$$

$$G_v^{(1)} = \frac{1}{2} [(R_{vxy} - R_{vyx})^2 + (R_{vxz} - R_{vzx})^2 + (R_{vzy} - R_{vyz})^2] \quad (4)$$

$$G_v^{(2)} = \frac{1}{2} [(R_{vxy} + R_{vyx})^2 + (R_{vxz} + R_{vzx})^2 + (R_{vzy} + R_{vyz})^2] \\ + \frac{1}{3} [(R_{vxx} - R_{vyy})^2 + (R_{vxx} - R_{vzz})^2 + (R_{vzz} - R_{vyy})^2] \quad (5)$$

Mineral name	Formula	mpid	Energy above hull (eV)	RRUFF ID
Billingsleyite	Ag <sub>7</sub> AsS <sub>6</sub>	mp-15077	0.003	R070350
Sanbornite	BaSi <sub>2</sub> O <sub>5</sub>	mp-3031	0	R060489
Hardystonite	Ca <sub>2</sub> ZnSi <sub>2</sub> O <sub>7</sub>	mp-6227	0.015	R040026
Perovskite	CaTiO <sub>3</sub>	mp-4019	0	R050456
Greenockite	CdS	mp-672	0	R090045
Cobaltite	CoAsS	mp-4627	0.001	R070372
Cobaltite	CoAsS	mp-16363	0.004	R060907
Cuprite	Cu <sub>2</sub> O	mp-361	0	R050374
Stromeyerite	CuAgS	mp-5014	0.024	R060908
Emplectite	CuBiS <sub>2</sub>	mp-22982	0	R070307
Chalcostibite	CuSbS <sub>2</sub>	mp-4468	0	R060262
Pyrite	FeS <sub>2</sub>	mp-226	0.008	R050070
Marcasite	FeS <sub>2</sub>	mp-1522	0	R060882
Langbeinite	K <sub>2</sub> Mg <sub>2</sub> (SO <sub>4</sub> ) <sub>3</sub>	mp-6299	0	R070285
Aphthitalite	K <sub>3</sub> Na(SO <sub>4</sub> ) <sub>2</sub>	mp-22457	0	R050651
Goldschmidtite	KNbO <sub>3</sub>	mp-7375	0	R190009
Nordite-(La)	Na <sub>3</sub> SrLaZnSi <sub>6</sub> O <sub>17</sub>	mp-13726	0	R140310
Swedenborgite	NaBe <sub>4</sub> SbO <sub>7</sub>	mp-8075	0	R060486
Leucophanite	NaCaBeSi <sub>2</sub> O <sub>6</sub> F	mp-560721	0	R050004
Neighborite	NaMgF <sub>3</sub>	mp-2955	0	R080108
Cotunnite	PbCl <sub>2</sub>	mp-23291	0.006	R060655
Matlockite	PbClF	mp-22964	0	R140538
Laurite	RuS <sub>2</sub>	mp-2030	0	R110120
Zincite	ZnO	mp-2133	0	R060027
Chrysoberyl	BeAl <sub>2</sub> O <sub>4</sub>	mp-3081	0	R040073
Wurtzite	ZnS	mp-10281	0.002	R130069
Montroydite	HgO	mp-1224	0	R070235
Quartz	SiO <sub>2</sub>	mp-7000	0.011	R050125
Bromellite	BeO	mp-2542	0	X050194
Litharge	PbO	mp-19921	0.001	R060959
Romarchite	SnO	mp-2097	0	R080006

Continued on next page

Table S1 – continued from previous page

Mineral name	Formula	mpid	Energy above hull (eV)	RRUFF ID
Anatase	TiO <sub>2</sub>	mp-390	0.006	R060277
Andalusite	Al <sub>2</sub> SiO <sub>5</sub>	mp-4753	0	R050258
Anglesite	Pb(SO <sub>4</sub> )	mp-3472	0	R040004
Aragonite	CaCO <sub>3</sub>	mp-4626	0.024	R040078
Baryte	Ba(SO <sub>4</sub> )	mp-3164	0	R040036
Brenkite	Ca <sub>2</sub> CO <sub>3</sub> F <sub>2</sub>	mp-6246	0.028	R060247
Calcite	CaCO <sub>3</sub>	mp-3953	0	R040070
Cerussite	Pb(CO <sub>3</sub> )	mp-19893	0	R040069
Colquiriite	CaLiAlF <sub>6</sub>	mp-1224	0	R070417
Dolomite	CaMg(CO <sub>3</sub> ) <sub>2</sub>	mp-6459	0	R050129
Eitelite	Na <sub>2</sub> Mg(CO <sub>3</sub> ) <sub>2</sub>	mp-6026	0	R110214
Eulytine	Bi <sub>4</sub> (SiO <sub>4</sub> ) <sub>3</sub>	mp-23331	0	R060058
Farringtonite	Mg <sub>3</sub> (PO <sub>4</sub> ) <sub>2</sub>	mp-14396	0	R130127
Geikielite	MgTiO <sub>3</sub>	mp-3771	0	R070479
Glauberite	Na <sub>2</sub> Ca(SO <sub>4</sub> ) <sub>2</sub>	mp-6397	0	R050350
Huntite	CaMg <sub>3</sub> (CO <sub>3</sub> ) <sub>4</sub>	mp-6524	0.004	R040126
Cristobalite	SiO <sub>2</sub>	mp-6945	0.003	R070235
Leiteite	ZnAs <sub>2</sub> O <sub>4</sub>	mp-29509	0.006	R040011
Lithiophosphate	Li <sub>3</sub> (PO <sub>4</sub> )	mp-2878	0.001	R100092
Magnesite	Mg(CO <sub>3</sub> )	mp-5348	0	R040114
Nahcolite	NaH(CO <sub>3</sub> )	mp-696396	0	R070237
Witherite	Ba(CO <sub>3</sub> )	mp-5504	0	R040040
Arsenolite	As <sub>2</sub> O <sub>3</sub>	mp-2184	0.009	R050383
Åkermanite	Ca <sub>2</sub> MgSi <sub>2</sub> O <sub>7</sub>	mp-6094	0.023	R061085
Benitoite	BaTi(SiO <sub>3</sub> ) <sub>3</sub>	mp-6661	0	R050320
Gahnite	ZnAl <sub>2</sub> O <sub>4</sub>	mp-2908	0	R070591
Rosiaite	PbSb <sub>2</sub> O <sub>6</sub>	mp-20727	0	R070384
Xanthoconite	Ag <sub>3</sub> AsS <sub>3</sub>	mp-561620	0	R070746
Topaz	Al <sub>2</sub> SiO <sub>4</sub> F <sub>2</sub>	mp-6280	0	R040121
Imiterite	Ag <sub>2</sub> HgS <sub>2</sub>	mp-9635	0.03	R080014
Acanthite	Ag <sub>2</sub> S	mp-610517	0.024	R070578
Argyrodite	Ag <sub>8</sub> GeS <sub>6</sub>	mp-9770	0	R050437
Andalusite	Al <sub>2</sub> SiO <sub>5</sub>	mp-4934	0.007	R050258
Nitrobarite	Ba(NO <sub>3</sub> ) <sub>2</sub>	mp-4396	0	R060622
Barylite	BaBe <sub>2</sub> Si <sub>2</sub> O <sub>7</sub>	mp-6383	0	R060620
Barylite	BaBe <sub>2</sub> Si <sub>2</sub> O <sub>7</sub>	mp-12797	0	R060606
Guanajuatite	Bi <sub>2</sub> Se <sub>3</sub>	mp-23164	0.028	R080140
Merwinite	Ca <sub>3</sub> Mg(SiO <sub>4</sub> ) <sub>2</sub>	mp-558209	0.038	R070195
Rankinite	Ca <sub>3</sub> Si <sub>2</sub> O <sub>7</sub>	mp-3932	0.009	R140775
Hurlbutite	CaBe <sub>2</sub> (PO <sub>4</sub> ) <sub>2</sub>	mp-6772	0	R090048
Rynersonite	CaTa <sub>2</sub> O <sub>6</sub>	mp-18229	0	R080064
Arsenopyrite	FeAsS	mp-561511	0	R050071
Gudmundite	FeSbS	mp-27904	0	R060741
Cinnabar	HgS	mp-634	0.004	R070532
Cinnabar	HgS	mp-9252	0.004	R070532
Kalsilite	KAlSiO <sub>4</sub>	mp-8355	0.002	R060801
Kalsilite	KAlSiO <sub>4</sub>	mp-9480	0.002	R060030
Avogadrite	KBF <sub>4</sub>	mp-4929	0	R110062
Kotoite	Mg <sub>3</sub> (BO <sub>3</sub> ) <sub>2</sub>	mp-5005	0	R060940
Natrosilite	Na <sub>2</sub> Si <sub>2</sub> O <sub>5</sub>	mp-3193	0	R060855

Continued on next page

**Table S1 – continued from previous page**

Mineral name	Formula	mpid	Energy above hull (eV)	RRUFF ID
Molybdomenite	PbSeO <sub>3</sub>	mp-20716	0	R140388
Valentinite	Sb <sub>2</sub> O <sub>3</sub>	mp-2136	0	R120096
Stibnite	Sb <sub>2</sub> S <sub>3</sub>	mp-2809	0	R120137
Moissanite	SiC	mp-7631	0	R150016
Tellurite	TeO <sub>2</sub>	mp-2125	0	R070606
Rutile	TiO <sub>2</sub>	mp-2657	0.037	R060745, R120008
Brookite	TiO <sub>2</sub>	mp-1840	0.02	R050363, R050591, R130225
Lorándite	TlAsS <sub>2</sub>	mp-4988	0	R110055
Tungstenite	WS <sub>2</sub>	mp-224	0	R070616
Waimirite-(Y)	YF <sub>3</sub>	mp-2416	0	R130714
Reinerite	Zn <sub>3</sub> (AsO <sub>3</sub> ) <sub>2</sub>	mp-27580	0	R080132
Baddeleyite	ZrO <sub>2</sub>	mp-2858	0	R100171

**Table S1.** Common structures in our database based on the same chemical formula and the mineral name in RRUFF compared to Materials Project tags. The bold RRUFF IDs refer to structures that have also similar lattice parameters.

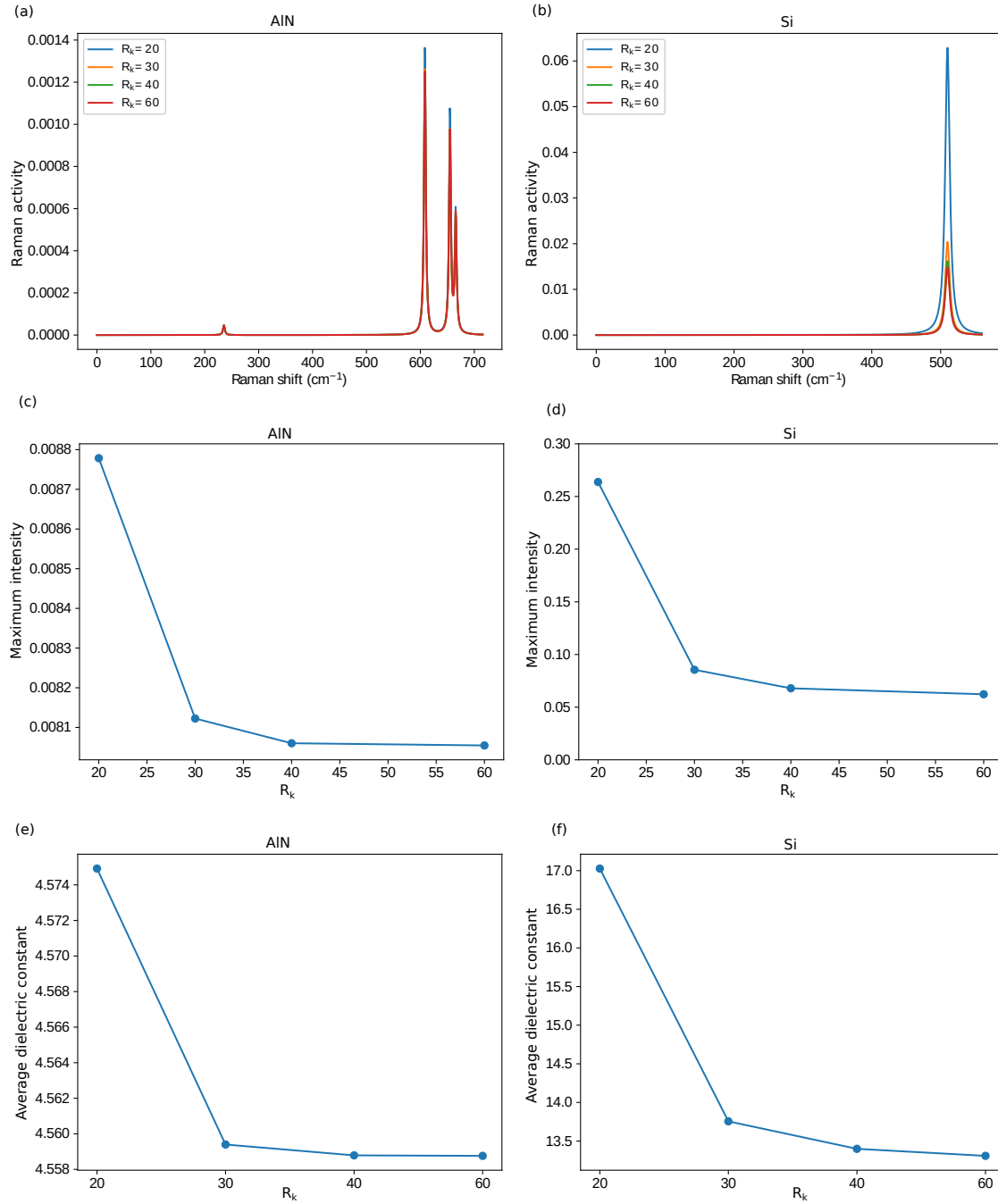


**Figure S1.** The effect of k-point mesh parameter  $R_k$ . (a) and (b) show the unnormalized Raman activity of AlN and Si, respectively, with  $R_k = 20$  (blue line), 30 (orange line), 40 (green line) and 60 (red line). (c) and (d) show the effects of different  $R_k$  on the maximum intensity of AlN and Si spectra, respectively. (e) and (f) show the effects of different  $R_k$  on the average dielectric constant of AlN and Si, respectively.

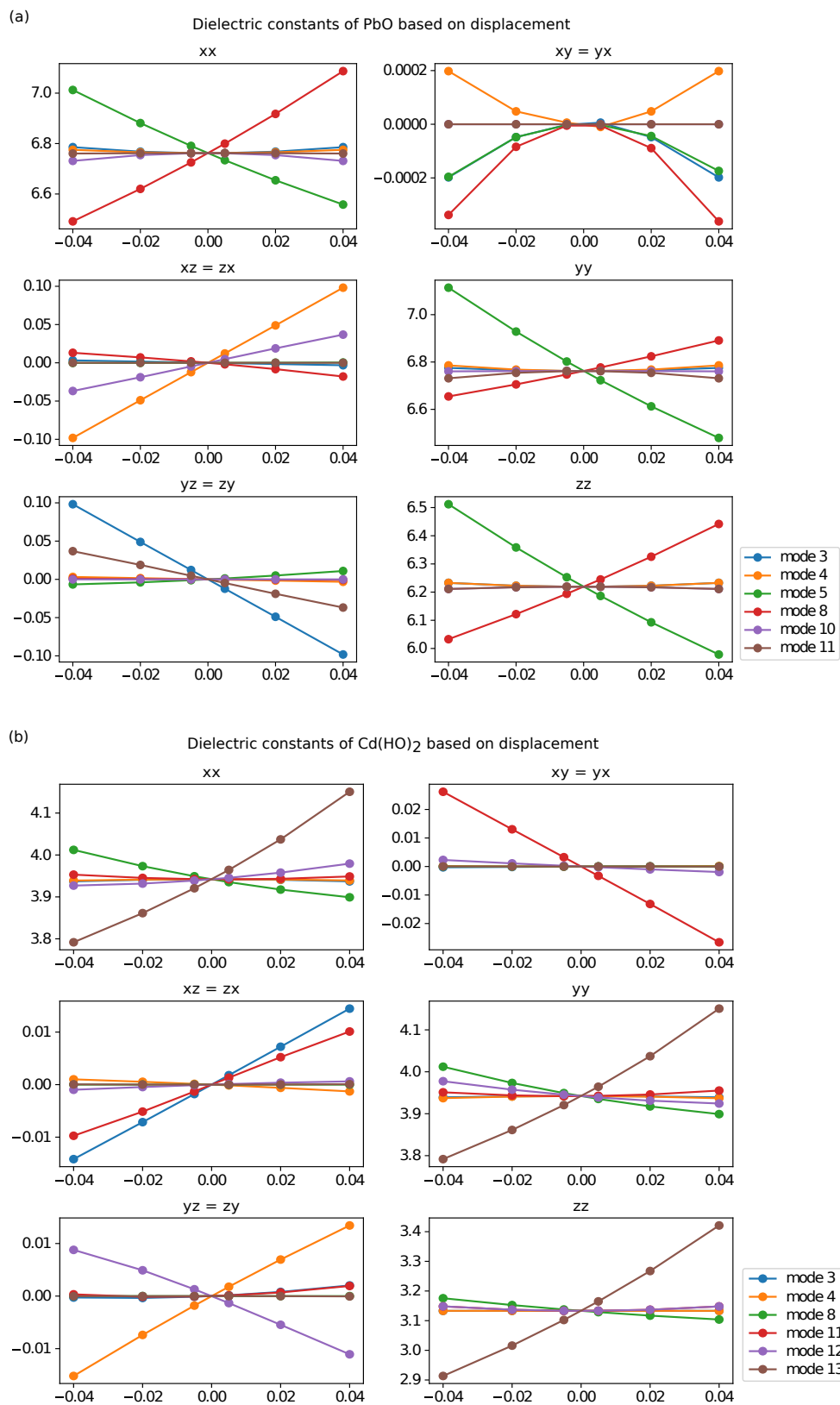


**Figure S2.** Changes of dielectric constant of (a) PbO and (b) Cd(HO)<sub>2</sub> in different directions as a function of the displacement step size (0.005–0.04).



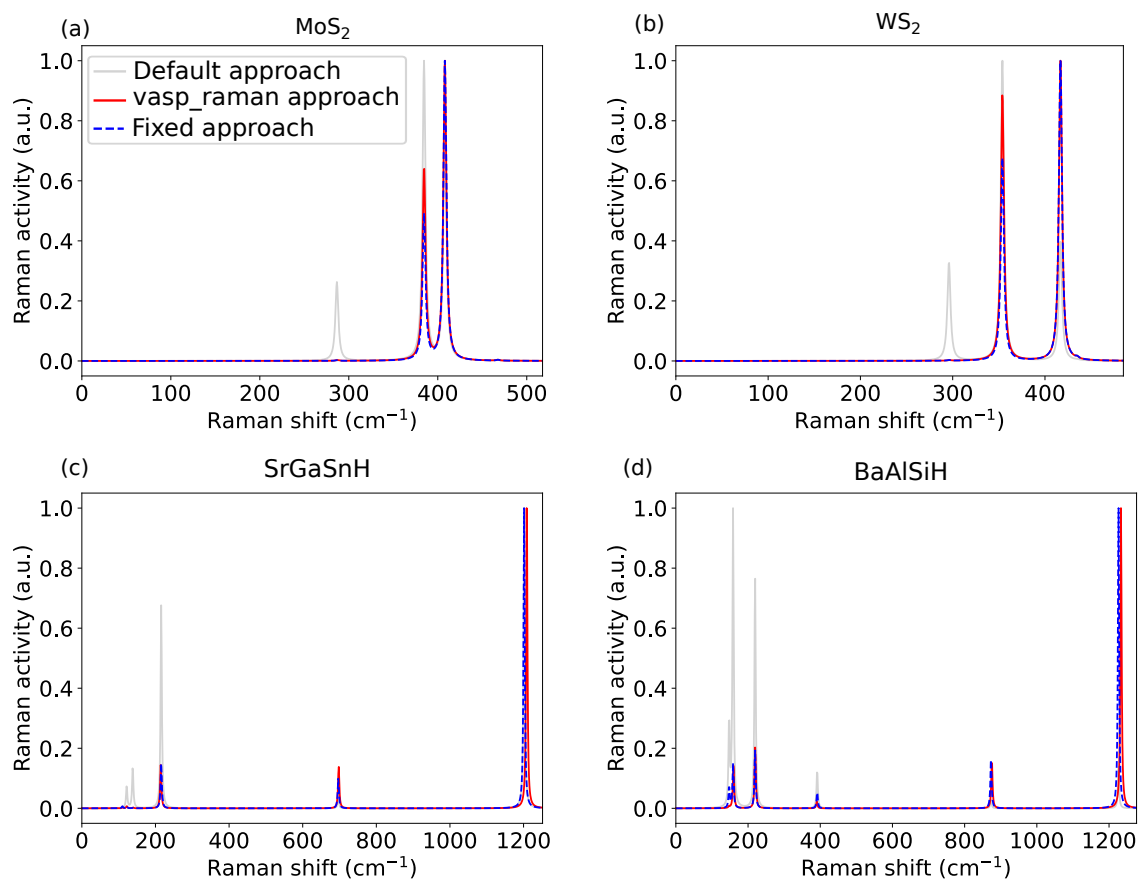


**Figure S3.** Comparison of the Raman activity from our workflow and that from vasp\_raman code. The spectra from old version of Atomate with incorrect eigenvector normalization is also shown.